Supporting Online Material for

Cortical network mechanisms of anodal and cathodal transcranial direct current stimulation in awake primates

Andrew R. Bogaard, Guillaume Lajoie, Hayley Boyd, Andrew Morse, Stavros Zanos, Eberhard E. Fetz

*To whom correspondence should be addressed: abogaard@uw.edu (A.R.B.)

The PDF file includes:

Materials and Methods

Data/Code availability statement

Supplemental Text

Supplemental Figures

Materials and Methods

Subjects and behavioral task. All experiments were conducted with two male Macaca nemestrina monkeys (S and W) and conformed to the National Institutes of Health 'Guide for the Care and Use of Laboratory Animals'. Procedures were approved by the University of Washington Institutional Animal Care and Use Committee.

Monkeys were trained in a visuomotor target tracking task conducted in a primate behavior booth equipped with a computer monitor (30 cm × 23 cm), tones for audio feedback, and a computer-controlled feeder dispensing fruit sauce as a reward. Monkeys voluntarily moved from the cage to a primate chair which was adjusted to allow each monkey to sit upright comfortably. The left arm was loosely restrained in a plastic tube, and the monkey used an isometric manipulandum with the right arm (contralateral to the recording array) to control the position of cursor on the screen using torque registered in two dimensions (flexion/extension, FE; radial/ulnar, RU). The head was restrained with flexible plastic bars for the duration of experiments to promote attention in the task and for stability of neural recordings.

There were four phases of each trial: OFF, START, CONTRACT, and RELAX. At the beginning of a trial, the screen was blank for five seconds (OFF), followed by a cue (START) that indicated the monkey would soon have to produce a torque about the wrist to one of eight possible targets (CONTRACT). During the START condition, the monkeys had to keep the cursor in a center target (no contraction) for a variable period of time (0.5-2 seconds) so that we could measure response time. During the CONTRACT condition, targets pseudo-randomly selected from one of eight targets in FE and RU were presented. After

holding the cursor in the CONTRACT target box for 1 second, the RELAX target would appear in the center of the screen, cueing the monkey to relax his wrist to receive a reward. The monkeys performed the task continuously for the entire duration of the experiment, and each experiment consisted of roughly 1000 trials.

Surgery and implants. Both monkeys underwent a two-stage implantation schedule. For all surgical procedures, the skin around the surgical site was shaved and scrubbed with betadine. Sterile surgery was performed with the animal under 1–1.5% isoflurane anesthesia (95:5 O2:CO2). Cardiac waveform, heart rate, respiratory frequency, blood-pressure and end-tidal CO_2 was monitored continuously. Post-operative care included recovery in a padded cage, administration of analgesics (ketoprofen 5 mg/kg), additional doses of antibiotics (cephalexin 25 mg kg−1 PO), and careful overnight observation by trained personnel. After recovery, monkeys showed no signs of discomfort related to any of the implanted devices.

During the first surgery, four 1.25x4mm perforated titanium craniofacial ties were affixed to the skull by 3 2x6mm titanium bone screws each. Two were implanted bilaterally over the occipital ridge, and two were placed temporally bilaterally. The plates integrated with the skull for 6 weeks and were used to reinforce the four points of contact for a halo system.

During the second surgery, the 96-channel microelectrode arrays (length = 1.5mm, Blackrock Microsystems, Salt Lake City, UT) were implanted (left M1, Monkey S; left SI, monkey W) using the pneumatic insertion technique[1]. To implant the array, a bone flap (1.5x1.5cm) was removed from an area of the skull located stereotactically. Electrode arrays were placed in hand/wrist sites in pre and postcentral gyrus, located in precentral gyrus from the line extending from the genu of the arcuate sulcus posteriorly to the central sulcus (Monkey S), or in the adjacent location in postcentral gyrus (Monkey W). After placement of the array, the dura was reapproximated over the array and the bone flap was replaced in the craniotomy with two 1mm screws and a single strip of thin titanium mesh plate together with hydroxyapatite to promote reintegration. At the end of experiments, the skull was inspected and there were no remaining defects or holes in the skull except for the hole permitting passage of the wire bundle.

One connector pedestal was fixed to the skull caudal to ear-bar-zero. Finally, a lightweight aluminum halo system used for head fixation and mounting the tDCS pads was mounted with four pins seated in each of the four bone straps implanted during the first surgery. These pins were low on the head and separated by >2 cm from the tDCS pads. Daily recording sessions began after the monkey had completely recovered from surgery.

Transcranial direct current stimulation. tDCS was designed to match human trials as closely as possible. Scalp pads were made from cellulose sponges soaked in 0.9% NaCl solution with inlaid copper wire, and were cut to a smaller size to accommodate the smaller anatomy of the monkey brain and skull (**Fig. 1d**; 3x3cm versus ~5x7cm. Sponges were checked so as to be moist throughout but not wet or dripping onto the scalp to avoid any undesired current spread. Similar to the classic sensorimotor cortex/contralateral supraorbital montage used in human trials[2,3], we used placed one pad over the implanted array in sensorimotor cortex (anode: a-tDCS, cathode:c-tDCS), and a second pad over the right supraorbital ridge (main text **Fig. 1c**). Proper location of pads was easily determined relative to landmarks (halo, pins, and connector pedestal) each day. As necessary, hair was removed with Nair™ (Church & Dwight Co.), and the was skin rinsed and dried. At the onset of tDCS, current was delivered by a programmable stimulator (IZ2, Tucker-Davis Technologies) or a manual stimulator as previously used in clinical trials (Phoresor II autostimulator, IOMED, Salt Lake City, UT) and was slowly ramped up over 1 minute to a predetermined current to decrease the chance of the animal perceiving the stimulation. Voltage delivered to the pads was monitored to ensure that the proper current was delivered throughout the experiment (i.e. proper pad contact and circuit impedance such that the compliance voltage of the stimulator was never reached). If noise was observed in the neural recording as tDCS current was ramped, stimulation was decreased to the nearest dose that did not affect recording (3 experiments). Similar to human trials[2], the duration of tDCS was 25 minutes, and we explored doses ranging from the lowest delivered to human subjects (0.027 mA/cm^2) to roughly four times the highest dose currently delivered to humans (0.44 mA/cm^2).

Experiment time course and behavioral task. During each experiment, the monkeys were transported from their home cage to the recording booth in a primate chair. Once in the booth, a feeder tube was placed in front of the monkey's mouth to deliver fruit sauce reward. Finally, we prepared the scalp and placed the tDCS pads (see **tDCS**, above), and connected the recording system to the microelectrode array.

At the start of the experiment, we initialized the behavioral task (custom MATLAB software), which ran without interruption until the experiment ended. Epoch 1 (Pre) lasted 20 minutes, and established baseline activity. Epoch 2 (Stim/Sham) lasted for 25 minutes, and had three possible conditions: a-tDCS, c-tDCS, or Sham. Epoch 3 (Post), lasted over 30 minutes, or until the monkey showed signs of fatigue or disinterest in the task. The monkeys often performed the task for up to an hour following tDCS.

In vivo neural recordings, task and behavioral data. We used a 256 channel digital data acquisition system (Tucker-Davis Technologies) to record neural, behavioral, and task data in the primate booth. Data from the manipulandum (isometric torque) and behavioral task (target number, cursor position, task condition) was sampled at 3kHz. Voltage signals from the microelectrodes were amplified, digitized, and streamed to the TDT base station with a sampling rate of 25kHz. The data streams from each electrode was processed and saved as local field potential (LFP) and single unit activity (SUA). To extract the LFP, signals were band-pass filtered (0.25 – 500 Hz), downsampled (3 kHz), and saved to hard disk. To extract SUA, signals were band-passed filtered (0.5-4 kHz), and a threshold unique to each channel was used to detect action potentials by negative threshold crossing. Thresholds were initially estimated automatically as minus three times the standard deviation estimated from 10 seconds of the SUA filtered signal, and the first five minutes of recording was used to ensure that thresholds were appropriately set outside of the baseline noise and to detect spikes. When a spike was detected, a snippet of SUA signal was recorded to the disk corresponding to 8 samples before the threshold crossing and 22 samples after the threshold crossing (1.2ms window)

Single unit identification and inclusion. Snippets of detected spikes in the SUA signal were sorted offline with Offline Sorter v4 (Plexon Co, Dallas, TX) using the template matching method. For each neuron, the signal to noise ratio (spike SNR)[4] was calculated by equation 1:

$$SNR = \frac{\max(\bar{W}) - \min(\bar{W})}{2 \cdot SD_{\varepsilon}}, (1)$$

where W the collection of all spike waveforms, $\bar{W}$ is the average waveform, and ε is the matrix of noise values calculated as deviations from the mean:

$$\varepsilon = W - \begin{bmatrix} \bar{W} \\ \vdots \\ \bar{W} \end{bmatrix} (2).$$

Only neurons with >1000 spikes, an average peak height of >50uV, and spike SNR >3 were included for analysis.

Statistical Analysis. All statistical comparisons were calculated using MATLAB R2017a. When applicable, we used paired statistical tests and did not assume normality. In particular, Wilcoxon's paired, two-sided sign rank test (signrank, MATLAB) was used when comparing cells across conditions, and the Wilcoxon's two sided rank sum test (ranksum, MATLAB) was used when comparing the behavioral and neural activity across sessions. Unless otherwise noted, data and error bars depict the median and the 95% confidence interval of the median, respectively.

Changes in firing rate. Data depicted in main text **Figure 2** was generated by compiling data across multiple experiments for each current step. The data from each individual experiment can be seen in **Supplemental Figure 2**. For these analyses, we calculated *ΔF,* which describes the percent change in firing between Pre and Post, and was calculated by equation 3:

$$\Delta F = 100 \ \frac{F_{Stim} - F_{Pre}}{\max(F_{Pre}, F_{PStim})}, (3)$$

where f_{Pre} and f_{Stim} are the median firing rates for the Pre and Stim/Sham epochs. Equation 1 is bound between -100 and 100.

We fit a sigmoid function to the data presented in Figure 2B, defined by equation 4:

$$\Delta F = \frac{A_M - A_0}{1 + 10^{b(x50 - x)}} + A_0, (4)$$

where A_0 is a fixed parameter defined by ΔF during Sham epochs for each monkey, and $A_M, x50$, and b are free parameters describing the maximal value, inflection point and inflection point slope, respectively.

Longitudinal cell identification. The microelectrode arrays used in these experiments are chronic, immovable, and can record stable SUA for years[5]. Therefore, it is likely that some neurons are recorded across many days. We leveraged this to investigate whether a-tDCS or c-tDCS reliably affected individual neurons across experiments. We performed an analysis inspired by previously reported work[6–8] to identify which spikes might originate from the same neuron across days using various spiking statistics (**Supplemental Figure 3)**. First, we calculated five metrics for each neuron: the mean waveform, spike rate during Pre, refractory period-timescale autocorrelation (bins logarithmically spaced from decades $10^{-3.6889}$ to 10^{-1}ms), regular-timescale autocorrelation (bins linearly spaced from 0 to 100ms), and ISI distribution (bins logarithmically spaced from decades 10^{-3} to $10^{1.5}$ms). Logarithmic spacing was used for short-timescale autocorrelation and ISI histogram so that the shape of short time interval features (where many important dynamics are reflected) were weighted similarly to slower ones.

The distance between each of the five metrics was calculated pairwise across all neurons. The L^2 norm was used for ISI distribution, autocorrelation, and firing rate, whereas the distance between spike waveforms was defined as 1 - sample correlation. The reason for this was the amplitude of the spike often changed day to day, but the shape generally did not, and the L^2 norm is sensitive to changes in amplitude, but the sample correlation is not. Each paired distance was z-scored for normalization, and we calculated the dot product between the four distances and a weighting vector **w** to favor the most distinctive features, namely the spike time autocorrelation and interspike interval distribution,

$$d_i = \vec{d}_i \cdot \vec{w}, \quad (5)$$

Where

$\bar{d} = [d_{waveform}, d_{ISI}, d_{ACORR1}, d_{ACORR2}, d_F]$, and $\bar{w} = [1, 1.3, 2, 2, 0.75]$

d was larger for neurons recorded on different channels than for neurons recorded on the same channel for both monkeys (**Supplemental Fig. 4c$_{i\text{-}ii}$**). This difference likely reflects that some neurons recorded across days were the same. We performed complete-linkage hierarchical clustering on the set of *d* for each channel, and clusters were cut from the cluster tree using a threshold for a distance criteria of 4 (see **Supplemental Fig. 4b)**, which corresponded to *d* most likely to be observed between neurons on the same channel as compared with neurons on different channels (**Supplemental Fig. 4c$_{i\text{-}ii}$**). Out of a total of 2671 neurons, the algorithm detected 1178 unique cells. **Supplemental Figure 5** shows how many neurons were recorded for a given number of sessions. **Supplemental Figure 6** shows channels with the most repeat recorded neurons detected by the algorithm.

Shuffle distributions for estimating statistical significance of repeated effects across sessions. For each condition (a-tDCS, c-tDCS, Sham), we calculated ΔF for all cells recorded more than once, and noted the percent of cells that were always modulated up or down past a given threshold *T*. We explored a range of *T* (from 0-10%) to avoid arbitrary parametrization. To determine whether repeat changes in ΔF were more consistent than statistically expected by chance alone, we shuffled all ΔF across cells recorded more than once during a given condition (10,000 iterations) to generate a distribution of percent of neurons with consistent ΔF for each *T*. Thus, we calculated the probability that observed repeat ΔF occurred by chance given the measured ΔF *in that condition*, thereby accounting for differences in ΔF across conditions (for instance, the chance level of repeat increases during a-tDCS is higher than c-tDCS because more cells tended to increase their firing).

Torque Directionality. Polar plots of firing rate by torque direction were generated to visualize the pattern of spiking dependent upon the animal's direction of wrist torque. To construct the rate map, torque direction was collected into bins of 6 degrees and the number of spikes in each bin was divided by the time the torque spent in that direction. To quantify the degree of directional selectivity, we calculated the mean resultant, R_m, of the directional firing rate map:

$$R_m = \frac{\cos(\bar{\theta})\sum_{i=1}^{n} F_i \cos(\theta_i) + \sin(\bar{\theta})\sum_{i=1}^{n} F_i \sin(\theta_i)}{\sum_{i=1}^{n} F_i}, \quad (6)$$

where $\bar{\theta}$ represents the preferred firing direction of the cell, and is calculated by

$$\bar{\theta} = \arctan\left(\frac{\sum_{i=1}^{n} F_i \sin(\theta_i)}{\sum_{i=1}^{n} F_i \cos(\theta_i)}\right), \quad (7)$$

Tuning rate functions. Firing rate maps of cell spiking in torque space were constructed by dividing the spike count within pixels of 2-dimensional torque data by the time spent by the cursor in that bin. Data were smoothed by a two-dimensional convolution with a pseudo-Gaussian kernel with a standard deviation of one pixel. Rate maps were compared across epochs using Pearson's correlation coefficient, ρ, calculated by the MATLAB function *corrcoef*. The torque vector information per spike was inspired by[9], and is defined in equation 8:

$$I = \sum_{i=1}^{N} p_i \frac{\lambda_i}{\lambda} log_2 \frac{\lambda_i}{\lambda}, \quad (8)$$

where the torque space was divided into N nonoverlapping pixels, p_i is the cursor occupancy probability of bin i, λ_i is the mean firing rate for bin i, and λ is the overall mean firing rate of the cell.

Spike-triggered LFP and unitary spiking contribution to LFP. We calculated whitened spike triggered LFP (wst-LFP) features as described by Teleńczuk et al[10]. The wst-LFP technique applies spatial filters that decorrelate LFP signals in space, thereby eliminating features such as beta oscillations that are broadly distributed across the array. After this filtering ("whitening") step, features in the spike-triggered averages are limited to electrodes adjacent to the triggering neuron, and peak at lag times that match predicted propagation speeds of axonal conduction. It appears that these features represent the unitary contribution of the single neuron to the LFP, reflected by post-synaptic currents following spikes.

The algorithm for calculating the wst-LFP has been described previously[10]. Briefly, the LFP was bandpass filtered (15-300Hz, 3rd order elliptic filter, results are similar with Butterworth), and we calculated the covariance matrix (*C*) of the continuous LFP across the 96 channels (some experiments and bad channels were removed by visual inspection). Averages of the ongoing LFP about spikes (st-LFP; -50 to 50 ms) are calculated for each cell, and the wst-LFP are calculated by the matrix product of the st-LFP and a whitening matrix (*W*) derived from the covariance matrix:

$$wstLFP_i = \sum_{j=1}^{96}(W)_{ij} \times stLFP_j, \quad (9)$$

where

$$W = E \times D^{-1/2} \times E^T, \quad (10)$$

and E is the matrix of eigenvectors of the covariance matrix, and D is a diagonal matrix of eigenvalues.

To calculate the change in wst-LFP trough about spiking, we averaged all electrodes separated from the triggering neuron position by the same L_1 (Manhattan) distance and took the minimum amplitude from lags 0-6ms relative to spike time. This window contains the full range of delays reported previously and observed in our data (main text **Fig. 7b**).

	High dose a-tDCS		*High dose c-tDCS*	
	N	λ_{pre}, λ_{post} *(mm)*	*N*	λ_{pre}, λ_{post} *(mm)*
All cells	111	0.21, 0.21	324	0.28, 0.28
FS	38	0.18, 0.24	107	0.37, 0.31
RS	73	0.33, 0.19	217	0.25, 0.24

Table 1. Fit parameters for Figure 7. The data is fitted with an exponential $A\ exp(-x/\lambda)+C$, where x is the distance and λ is the space constant. N_{cells} for this analysis are less than for others because some experiments were omitted due to poor LFP signal quality (N omitted, Sham: 8, a-tDCS: 10, c-tDCS: 15)

Neural population dynamics dimensionality reduction and analysis. Population spiking activity during the target tracking task was analyzed with a focus on neural dynamics surrounding each cursor movement.

Supplemental Figure 7a shows data for an example trial where time $t = 0$ when the target appears on screen. The top panel of **Supplemental Figure 7a** shows the *FE*- and *RU-torques* registered by the manipulandum while the second panel shows a raster plot of spike times for all recorded neurons ($N = 49$) during that experiment. Similar to other studies[11], the instantaneous firing rate of each neuron is approximated by convolving its spike train with a Gaussian filter with $\sigma = 100$ milliseconds and temporal resolution of $dt = 1$ millisecond, as illustrated in the third panel in **Supplemental Figure 7a**. We verified that changing the definition of instantaneous rate did not change the qualitative nature of our results by testing one-sided Gaussian and Exponential filters, as well as spike counts in sliding windows of width σ ranging from 10-100ms. On each trial, the firing rate curve of every neuron was normalized to zero mean and unit variance (over the time course of the trial) to mitigate the biasing effects heterogeneous spike counts across neurons and tDCS induced changes. Neural population activity during trials was thus described by a time-dependent, N-dimensional rate vector, as depicted in the bottom panel of **Supplemental Figure 7a** (not normalized for illustration). The trial-averaged mean firing rate of a neuron was computed by averaging the rates at each time point across aligned trials. Target-conditioned mean rates were obtained by only including trials with the same target in the averaging. **Supplemental Figure 7b** shows the mean rate aligned on target 1, for two example neurons (one is up-modulated and the other is down-modulated). For all following analysis, only the activity taking place between $t = 0$ (target onset) and $t = 0.5$ seconds was considered. **Supplemental Figure 7c** shows the mean rates of all neurons ($N_{cells} = 49$) for each target.

Rate averaging was further conditioned on the four experimental epochs (Pre, tDCS/Sham, Post). We performed a principal component analysis (PCA) of neural dynamics for each epoch by concatenating all target-conditioned mean rates vectors into a large set of N_{cell}-dimensional vectors. This procedure is a version of demixed PCA[12,13] and extracts relevant subspaces where population coding takes place by taking task parameters into account. **Supplemental Figure 8** illustrates the results of this analysis for three experimental sessions with different tDCS modalities (sham, a-tDCS, c-tDCS) where we plot the

projection of the target-conditioned population rates in the space spanned by the first two principal components (PC), alongside the target-conditioned mean torques for the corresponding tDCS epochs (**Supplemental Fig 8a**). Thus, for each epoch, a different PCA model was computed. Even if the shape of projected activity differed from one model to the next, the first two PCs were often sufficient to decode direction of motion for any tDCS modality since the task has two degrees of freedom. To check this, we trained a linear classifier to predict target from the single-trial activity projected in the first two demixed PCs and found that the average of the 80%-20% split, cross-validated performance was between 80% and 95% (close to monkey performance) for all sessions. Trials where the monkey failed to reach the appropriate target were included in this spot check.

We estimated the dimensionality of ensemble trajectories using previously reported methods[14,15]. The dimension *D* of a set of points in *N* dimensions is computed as:

$$D = \frac{\left(\sum_{i=1}^{N} \mu_i\right)^2}{\sum_{i=1}^{N} {\mu_i}^2}, \quad (11)$$

where μ_i represents the eigenvalues of the covariance matrix of the data used in the PCA model. If the *N* coordinates are statistically independent from one another, *D*=*N,* and if they are perfectly correlated, *D*=1.

To quantify how individual neurons contributed to a subspace spanned by a given set of PCs, we defined the neuron's ***participation score***: the norm of the canonical neural vector v_i (*N*-dimensional vector with zeros everywhere but at the i^{th} position) linearly projected in the subspace. **Supplemental Figure 8c** shows the participation score of all *N* neurons for the space spanned by the first two PCs in each epoch-specific PCA models (neurons are ordered by their participation score in the *PRE* model). Some neurons were more informative than others, and the spread in participation scores reflects that. In contrast, if all neurons contributed equally to the subspace, their scores would all be $\sqrt{d/N}$ where *d* is the dimension of the subspace ($1 \leq d \leq N$, see dashed line in **Supplemental Figure 8c**). For a given subspace dimension *d*, we measured the difference in participation scores between two epoch-specific PCA models by computing the Pearson correlation coefficient, C_{part}, of the pairs $\{(s(d)_i^a, s(d)_i^b)\}_1^N$ where $s(d)_i^a$ denotes

the participation score of neuron i in the first d-dimensions of PCA model a. A high correlation coefficient indicates that neurons have similar participation scores in models a and b, while a low coefficient indicates a big change in participation. Variability in participation score is expected between epochs, even for sham sessions where no stimulation is administered since neural activity is noisy and drifts during the course of the experiment. This is especially true for $d \ll N$ since low-dimensional subspaces have many "free degrees of freedom" to move in (i.e. N-d). Nevertheless, we concentrate on d=2 since the task itself involves two degrees of freedom (i.e x- and y-torques), a fact that should be recovered in task-relevant neural activity. We find that tDCS stimulation can induce greater-than-normal variability in participation score for d=2, indicating a rearrangement of neurons' roles in supporting task-relevant subspace (see statistical tests reported in **Supplemental Figure 9**). We verified that these results generally hold for d up to 5.

Beyond the contribution of neurons to coding subspaces, we investigated the geometry of subspaces themselves. PCA produces linear subspaces (hyperplanes) whose orientation can be measured by principal angles. To measure how similarly oriented are two d-dimensional PC subspaces, we measured the d principal angles between them $\{\theta_1, \dots, \theta_d\}$ and define their ***orientation similarity***, S_{ori}, as the mean cosine of these angles: $\frac{1}{d}\sum_{i=1}^{d}\cos(\theta_i)$. Identical subspace will have S_{ori} = 1, while orthogonal spaces will have S_{ori} = 0 (see **Supplemental Figure 9**).

We computed the three comparative quantities described above, (i) explained variance ratio difference, D_{var}, (ii) correlation of participation score, C_{part}, and (iii) orientation similarity, S_{ori}, for three tDCS epoch pair combinations (*Pre-Stim, Pre-Post)* across experiments with different tDCS current doses (low dose ≤1mA and high dose >1mA).. Comparison between tDCS and Sham experiments were made using independent t-tests. The number of neurons N varied from session to session and we discarded any session with N<10 (experiments included; Monkey S: 59, Monkey W: 40), with N ranging from 10 to 54 with median of 27. Results for both monkeys were similar, and we combined experiments to increase

power for statistical analysis. The following table further breaks down the number of samples by session type:

	anodal	cathodal	sham
low dose	n=14	n=14	n=40
high dose	n=13	n=18	

Table 2. Number of experiments for each population dynamics analysis

Supplemental Figure 9 shows box plots of all sampled quantities along with these p-values.

Data/Code availability statement

The data and code that support the findings of this study are available from the corresponding author upon reasonable request.

Supplemental text

Limitations While we tried to match human tDCS as closely as possible, some differences were unavoidable: to record intracortically requires a bone defect where the recording electrode wire bundle passes into the intracranial space, and we used a thin titanium strap to hold the bone flap in place immediately post implantation. Implants and boney defects may distort the electric field or shunt current. On the other hand, we found that the bone flap reintegrated fully, the residual passage for the wire bundle was very small, and extracranial tissue recovered fully. Furthermore, the skull itself is naturally porous due to features like cranial sutures and Haversian canals, and the relatively snug passage for the wire bundle may not be so different.

Another reason these numbers cannot be directly projected to humans is that the monkey and human head and skull are significantly different: human skulls are thicker than monkey skulls, and hair is often left in place during human experiments, whereas we removed it. Future work may compare the predicted intracranial electric field intensity using finite element head models of monkeys and humans. It is worth noting that despite these differences, a recent human trial tested a range of currents outside of normal tDCS, and the lowest current density that produced changes (in EEG alpha oscillations) was similar to

that which produced significant single cell effects in our study[16] (0.125mA/cm^2 versus 0.11mA/cm^2). Finally, while the two-pad form of tDCS is still the most common, newer types of tDCS exist that may be more targeted and effective[16–19].

Supplemental figures

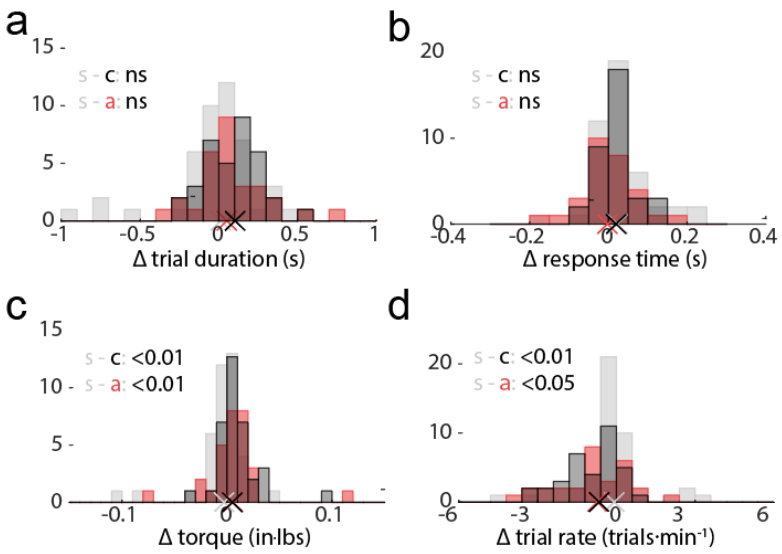

Supplemental figure 1. Task performance and behavior during tDCS and Sham. Each plot shows histogram of changes for a given performance metric from Pre to Stim/Sham, with the median indicated along the x-axis with an 'X' (Sham: light gray, a-tDCS: red, c-tDCS:black). There was no difference between the time it took monkeys to complete trials (trial duration, $p>0.05$, **a**), or the time it took monkeys to move the cursor to the target following the variable hold period (response time, $p>0.05$, **b**). There was a small but significant difference between the changes observed during tDCS and Sham for the median torque produced during trials (**c,** median Δtorque, Sham=-2.9e-3 in·lbs, a-tDCS = 5.7e-3, c-tDCS = 5.2e-3) and number of successful trials per minute (**d**, trials with duration <6secs, Sham=-0.08 trials/min, a-tDCS =-0.72, c-tDCS =-0.6). Overall, behavior was tightly controlled during tDCS and was similar across experiments, because the monkeys were overtrained and completed the task at peak performance. Regular performance was important to eliminate any potential confounds associated with behavioral changes.

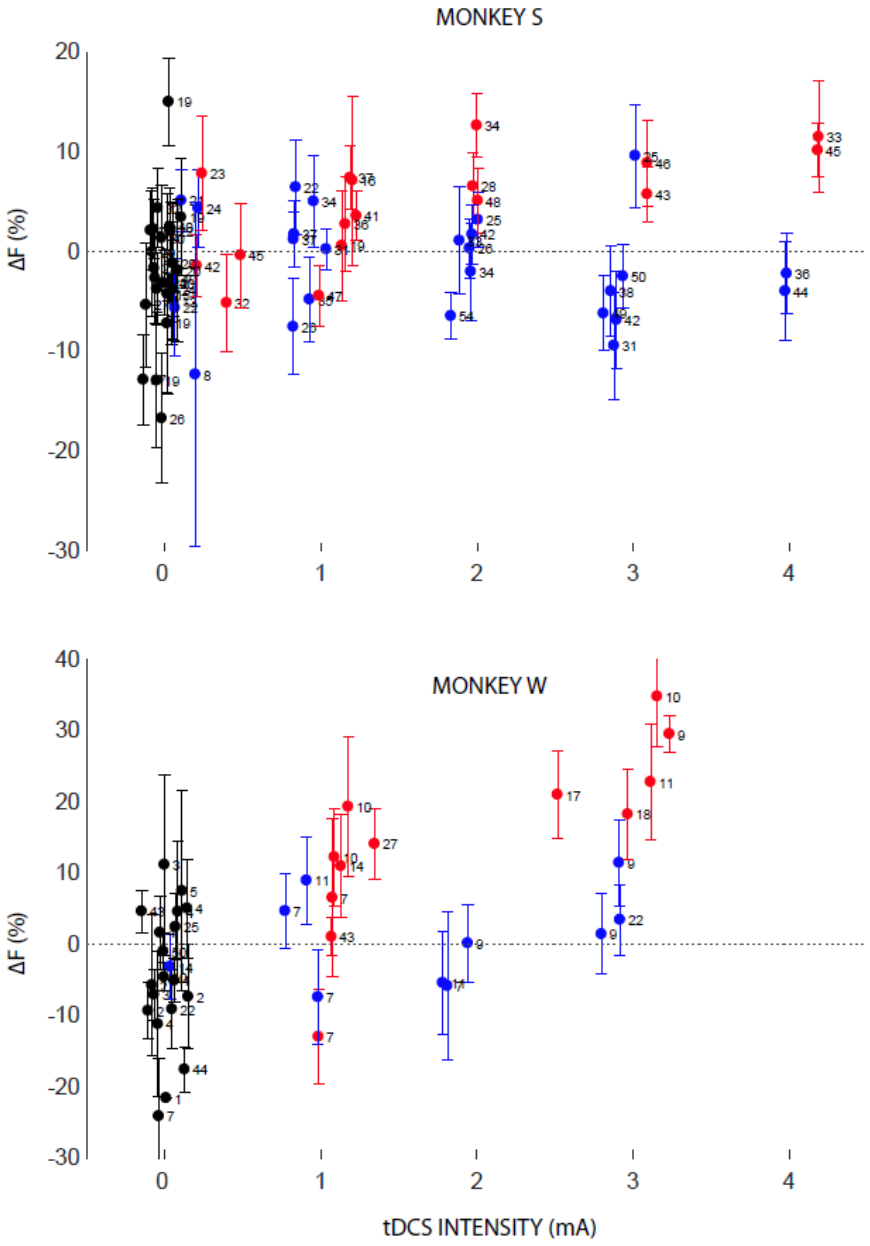

Supplemental figure 2. Average change in spiking for every experiment. Data plotted is mean ± standard error, and the number of neurons recorded is indicated in parentheses.

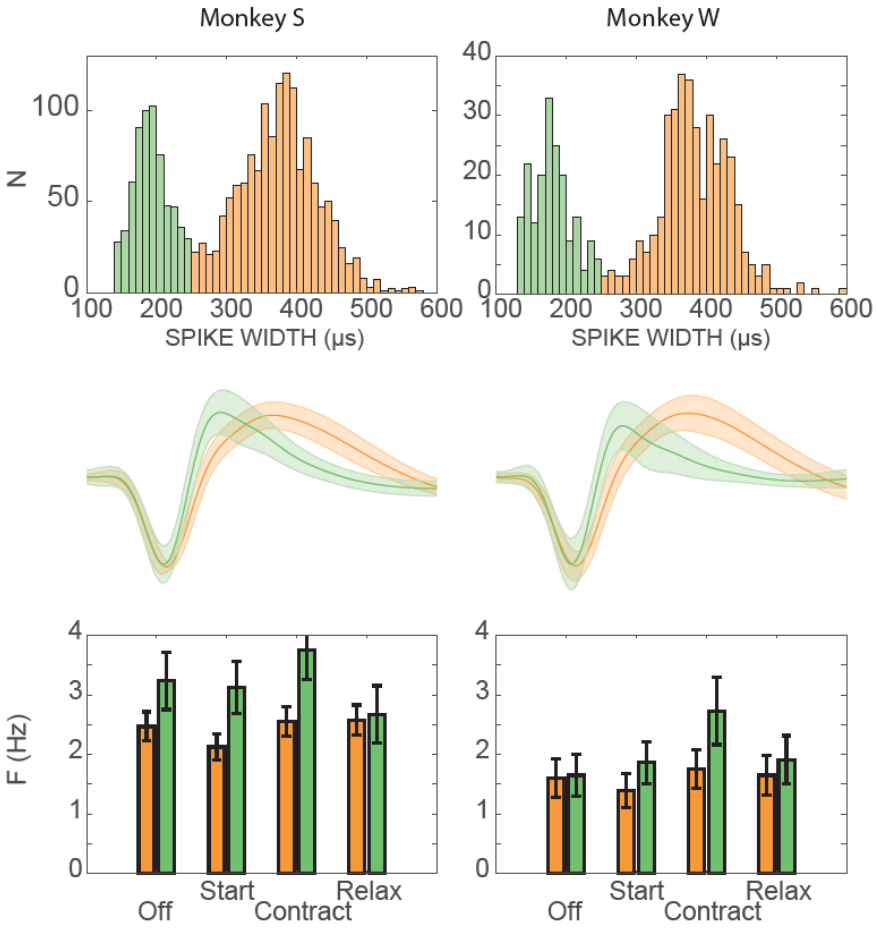

Supplemental figure 3. Population composition of FS and RS cells. Both monkeys had comparable ratios of RS:FS cells. Top: distribution of waveform width across all cells recorded in each monkey. Middle: average waveform and standard error for FS (green) and RS (orange) cells. Bottom: Median firing rates ± 95% confidence interval for RS and FS cells during four task periods. Consistent with other studies, RS cells fired less than FS cells overall. Modulation of firing by cell type was consistent in both monkeys.

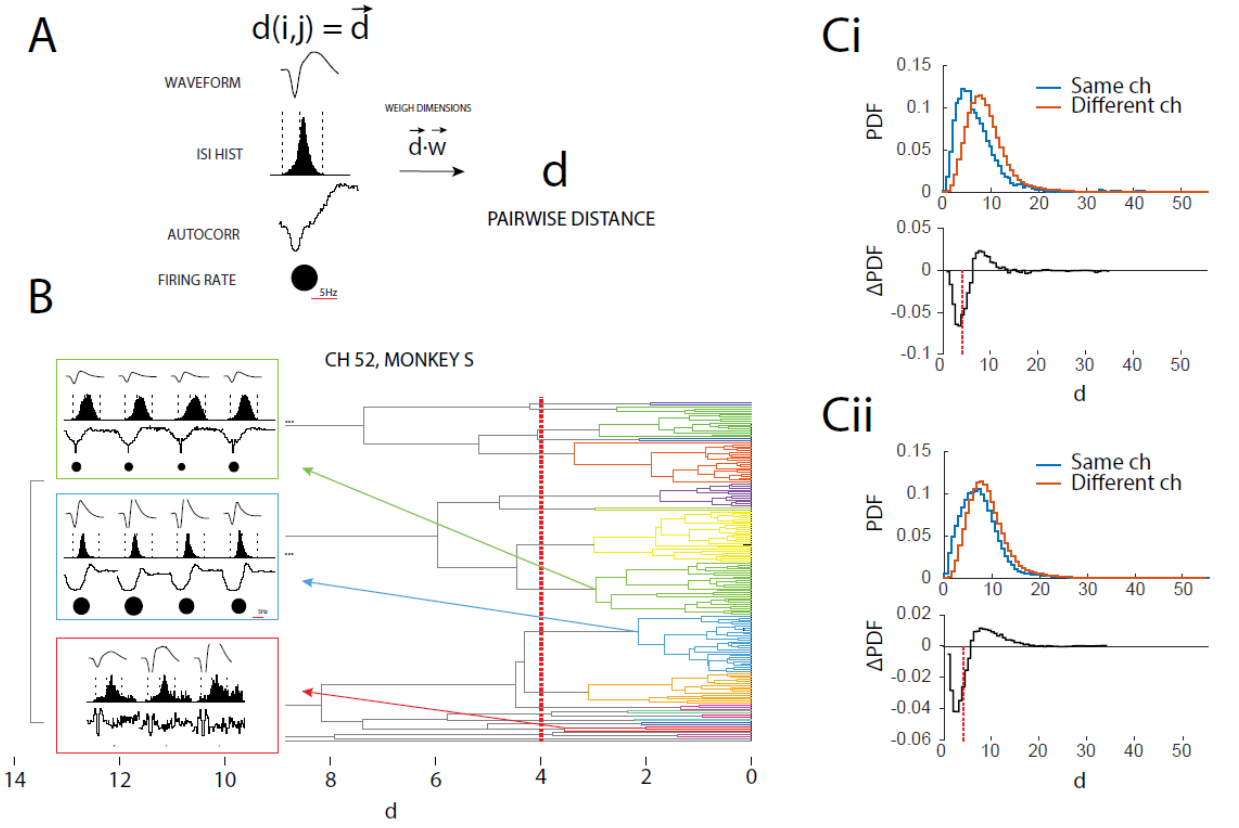

Supplemental figure 4. Algorithm for longitudinal cell identification. **(a)** Five statistics of firing were calculated for each neuron during Pre, including average waveform shape, inter-spike interval histogram, spike-time autocorrelogram at two timescales, and average firing rate. We calculated pairwise differences for each metric across all recorded neurons, z-scored difference measure, and weighted the combined difference vector **d** by **w** to weight certain factors, such as autocorrelation, more heavily. **(b)** Example clustering results for a single recording channel over many experiments. We performed complete-linkage hierarchical clustering on the weighted set of *d* for each channel, using a distance threshold criteria of 4 derived from distributions shown in **(c)**. **(c)** Distribution of *d* between neurons recorded on the same channel (blue line) and neurons recorded on different channels (red line) in Monkey S **(i)** and Monkey W **(ii)**. There is a higher frequency of low *d* between neurons recorded on the same channel, reflecting the fact that some neurons are repeatedly recorded during separate experiments. We derived the cluster threshold cutoff using these two distributions, selecting a value (4) that corresponded to the *d* most likely to be observed between neurons on the same channel as compared with neurons on different channels.

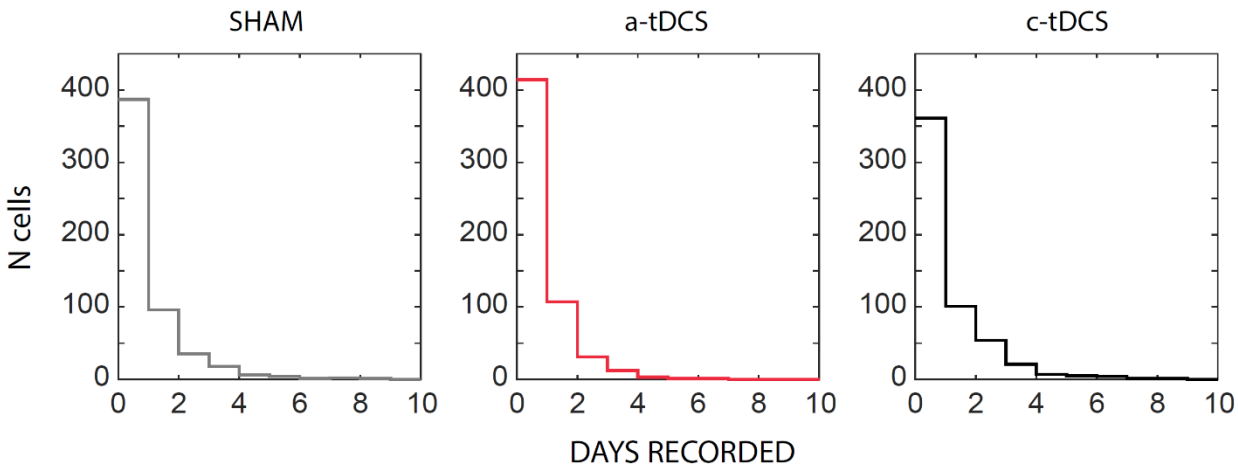

Supplemental figure 5. The number of cells recorded across sessions was similar for all conditions as detected by longitudinal cell tracking algorithm. Most neurons were recorded only once for a given condition (N=1162), but each condition (a-tDCS, c-tDCS, Sham) had a sizable number of neurons recorded more than once. These neurons permitted estimation of the reliability of tDCS effects in single neurons across sessions.

Supplemental figure 6. Results of longitudinal cell identification algorithm. Exemplary channels with unusually high repeat neurons are shown. Each neuron is represented by four statistics (Scale bars in top left. From top to bottom: average waveform, average firing rate (grey circle), inter-spike interval histogram, spike time autocorrelation.) Neurons identified across sessions are plotted together in boxes.

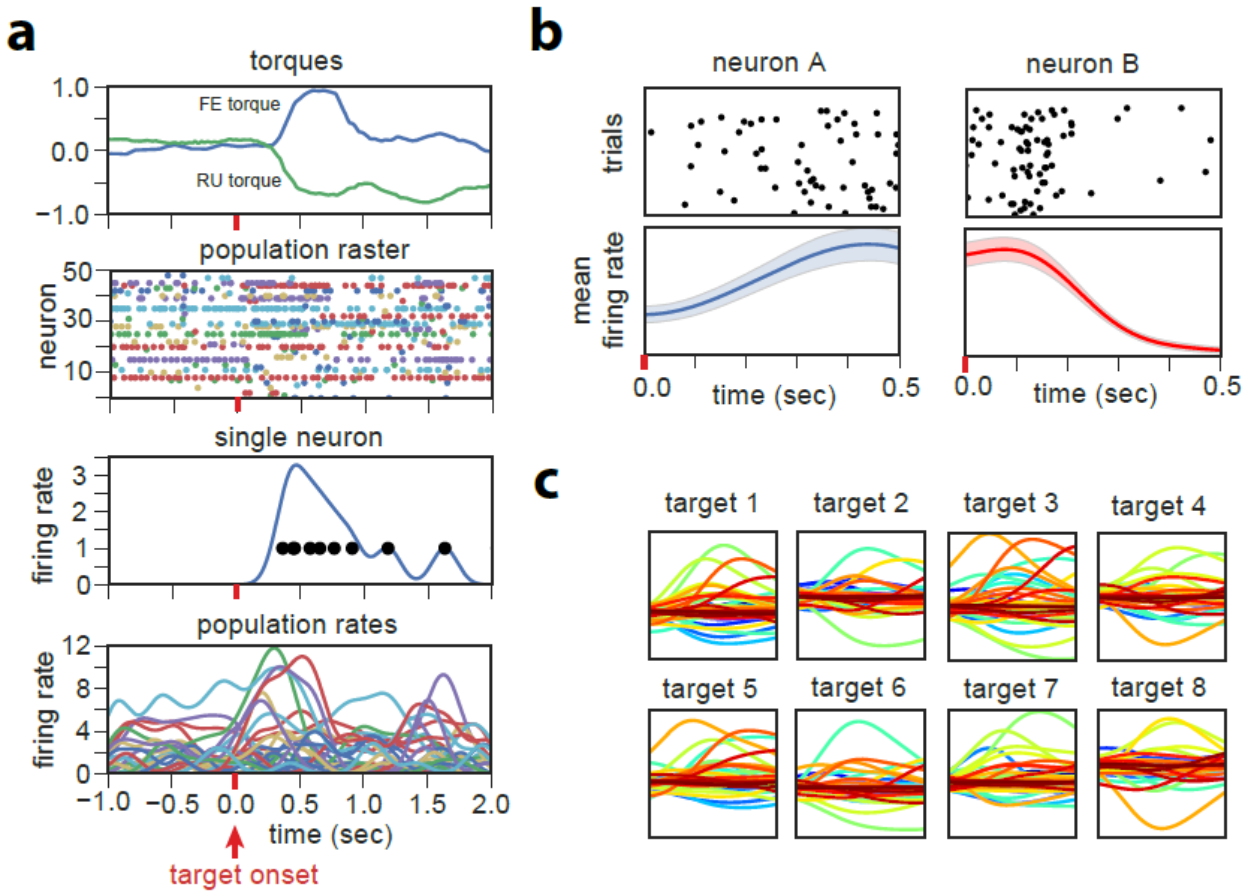

Supplemental figure 7. Task-specific population dynamics. **(a)** Example dynamic quantities for a target tracking task (N=49 neurons). Target onset occurs at t=0 (red bar on time axis). Top panel: manipulandum x- and y-torque trajectories. Second panel: population raster plot, each dot represents a spike time. Third panel: spike times of single neuron (black dots) and Gaussian-filtered rate (σ=100 milliseconds). Bottom panel: population firing rate curves as in third panel, colors match those of second panel (not normalized for illustration). **(b)** Target-specific, cross-trial spiking for two example neurons. Top: cross-trial raster plot. Bottom: mean firing rate curve. Shaded area shows one standard error of the mean. **(c)** Population mean firing rate curves (each color indicates a specific neuron) separated by target number for same time interval as (b).

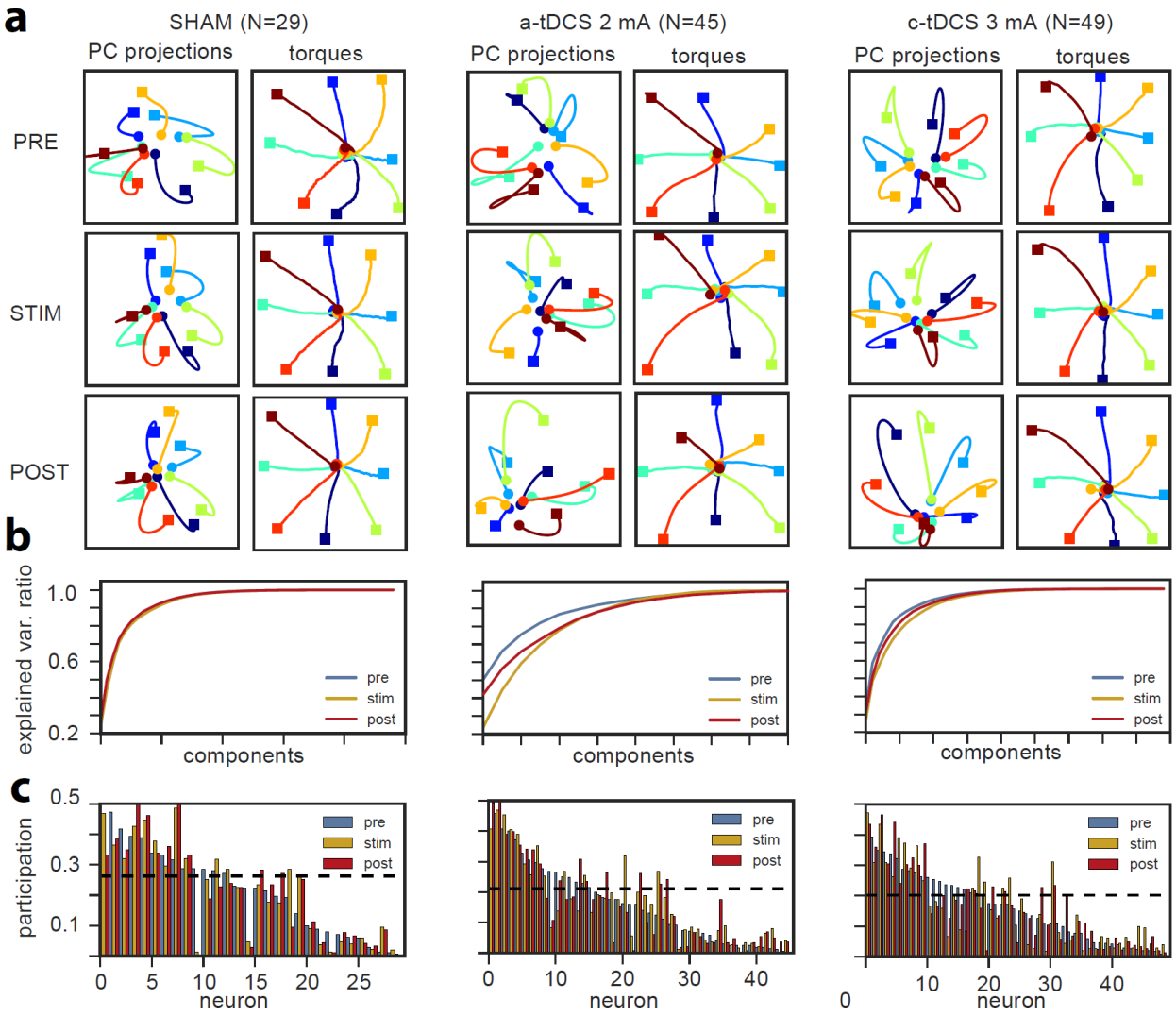

Supplemental figure 8. Examples of ensemble trajectories in 2D manifold. PCA–related quantities for three representative sessions. **(a)** Sham, N=29. **(b)** A-tDCS (2 mA), N=45. **(c)** C-tDCS (3 mA), N=49. Top three rows (for all panels): Target-specific, averaged population firing rates projected in first two PCs (left) and averaged manipulandum torques (right). Each row indicates tDCS epoch (Pre, Stim, Post). Colors indicate target identity, circle markers indicate t=0 seconds (target onset), square markers indicate t=0.5 seconds. **(b)** Explained variance ratio curves from PCA. **(c)** *Participation scores* of all neurons, for subspaces spanned by first two PCs (d=2) of PCA models PRE, STIM and POST, respectively. Neurons are ordered in decreasing order of score in model PRE. Dotted line indicates score that equally participating neurons would hold.

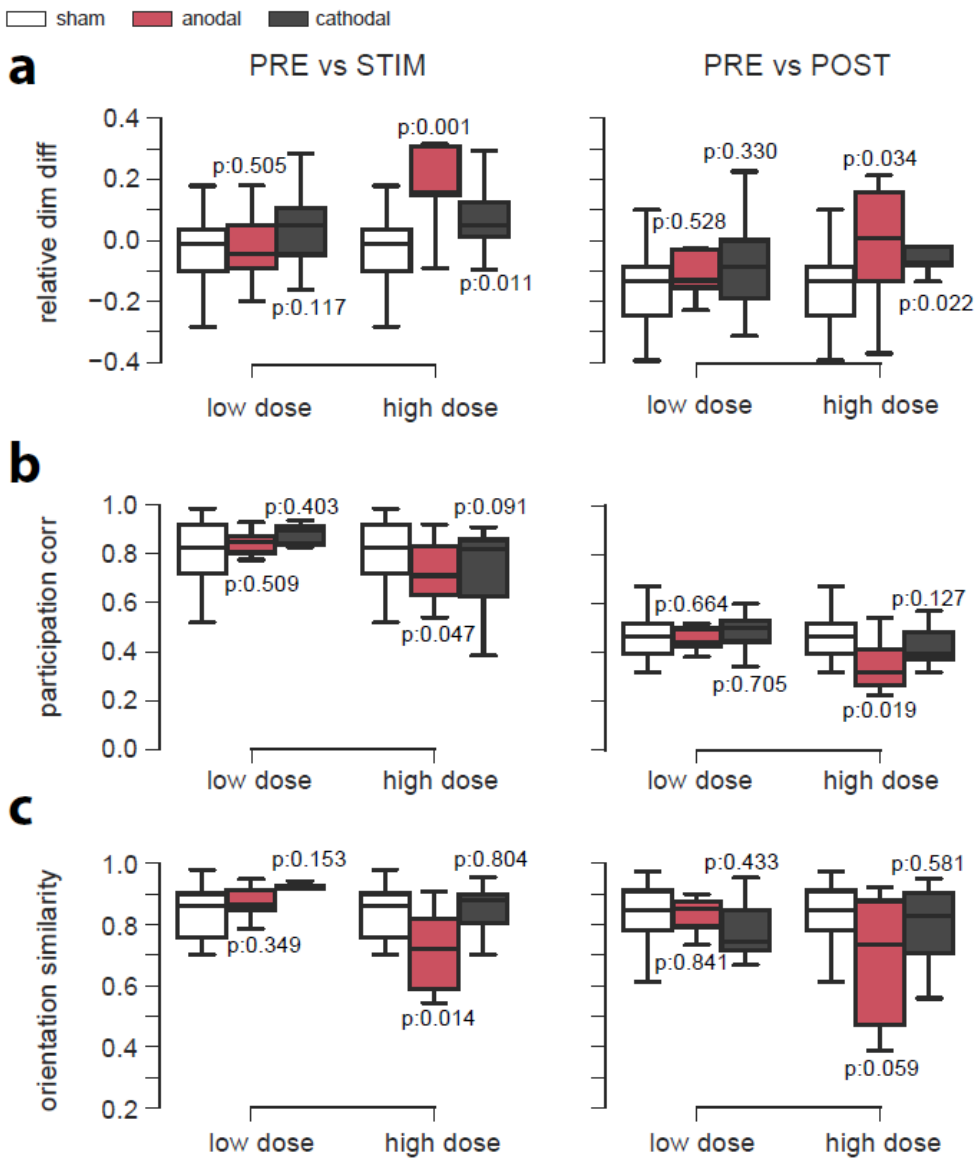

Supplemental figure 9. Statistics of population coding metrics. **(a)** Change in dimensionality of ensemble trajectories. Dimensionality is normalized by Pre to account for differences across experiments. Main Figure 6 shows pre-normalization values. **(b)** Correlation coefficient for participation score of neurons to the subspace spanned by the first two (d=2) PCs of PCA models. **(c)** Orientation similarity measure between subspace spanned by first two PCs (d=2) of PCA models. For all panels: Box edges show first and third quartiles, internal bar shows mean, whiskers show extremal values. Comparative quantities are plotted for model pairs. From left to right: Stim-Pre, Post-Pre. In each plot, quantities are shown for tDCS low (≤ 1mA, left) and high (>1mA, right) doses, for three conditions: sham (white), a-tDCS (red), c-tDCS (black). Sham box is repeated for low and high doses. P-values are computed from comparison with sham samples with an independent t-test. Effects during Post reflect activity for 30 minutes after tDCS was turned off.

Supplemental References

1. Rousche, P. J. & Normann, R. A. A method for pneumatically inserting an array of penetrating electrodes into cortical tissue. *Ann. Biomed. Eng.* **20,** 413–422 (1992).

2. Elsner, B., Kugler, J., Pohl, M. & Mehrholz, J. Transcranial direct current stimulation (tDCS) for improving function and activities of daily living in patients after stroke. *Cochrane Database Syst. Rev.* **2013,** Cd009645 (2013).

3. Lindenberg, R., Nachtigall, L., Meinzer, M., Sieg, M. M. & Floel, A. Differential effects of dual and unihemispheric motor cortex stimulation in older adults. *J Neurosci* **33,** 9176–9183 (2013).

4. Kelly, R. C. *et al.* Comparison of Recordings from Microelectrode Arrays and Single Electrodes in the Visual Cortex. *J. Neurosci.* (2007). doi:10.1523/JNEUROSCI.4906-06.2007

5. Simeral, J. D., Kim, S.-P. P. S.-P., Black, M. J., Donoghue, J. P. & Hochberg, L. R. Neural control of cursor trajectory and click by a human with tetraplegia 1000 days after implant of an intracortical microelectrode array. *J Neural Eng* **8,** 25027 (2011).

6. Fraser, G. W. & Schwartz, A. B. Recording from the same neurons chronically in motor cortex. *J. Neurophysiol.* **22,** 11–17 (2012).

7. Richardson, A. G., Borghi, T. & Bizzi, E. Activity of the same motor cortex neurons during repeated experience with perturbed movement dynamics. *J. Neurophysiol.* **107,** 3144–54 (2012).

8. Vaidya, M. *et al.* Ultra-long term stability of single units using chronically implanted multielectrode arrays. *Conf. Proc. ... Annu. Int. Conf. IEEE Eng. Med. Biol. Soc. IEEE Eng. Med. Biol. Soc. Annu. Conf.* (2014). doi:10.1109/EMBC.2014.6944715

9. Abeles, M., Goldstein, M. H., Skaggs, W. E. & McNaughton, B. L. Theta Phase Precession in Hippocampal Neurinak Populations abd the Compression of. *Hippocampus* **6,** 149–172 (1996).

10. Telenczuk, B. *et al.* Local field potentials primarily reflect inhibitory neuron activity in human and monkey cortex. *Sci. Rep.* **7,** (2017).

11. Churchland, M. M. *et al.* Neural population dynamics during reaching. *Nature* **487,** 51–56 (2012).

12. Brendel, W., Romo, R. & Machens, C. K. Demixed Principal Component Analysis. *Adv. Neural Inf. Process. Syst. 24* 2654–2662 (2011).

13. Kobak, D. *et al.* Demixed principal component analysis of neural population data. *Elife* (2016). doi:10.7554/eLife.10989

14. Litwin-Kumar, A., Harris, K. D., Axel, R., Sompolinsky, H. & Abbott, L. F. Optimal Degrees of Synaptic Connectivity. *Neuron* **93,** 1153–1164.e7 (2017).

15. Mazzucato, L., Fontanini, A. & La Camera, G. Stimuli Reduce the Dimensionality of Cortical Activity. *Front. Syst. Neurosci.* **10,** (2016).

16. Vöröslakos, M. *et al.* Direct effects of transcranial electric stimulation on brain circuits in rats and humans. *Nat. Commun.* **9,** (2018).

17. Edwards, D. *et al.* Physiological and modeling evidence for focal transcranial electrical brain stimulation in humans: A basis for high-definition tDCS. *Neuroimage* (2013). doi:10.1016/j.neuroimage.2013.01.042

18. Grossman, N. *et al.* Noninvasive Deep Brain Stimulation via Temporally Interfering Electric Fields. *Cell* **169,** 1029–1041 (2017).

19. Luu, P. *et al.* Slow-Frequency Pulsed Transcranial Electrical Stimulation for Modulation of Cortical Plasticity Based on Reciprocity Targeting with Precision Electrical Head Modeling. *Front. Hum. Neurosci.* (2016). doi:10.3389/fnhum.2016.00377